

# 3-D Image Reconstruction from Averaged Fourier Transform Magnitude by Parameter Estimation

Yibin Zheng, *Member, IEEE*, and Peter C. Doerschuk, *Member, IEEE*

**Abstract**—An object model and estimation procedure for three-dimensional (3-D) reconstruction of objects from measurements of the spherically averaged Fourier transform magnitudes is described. The motivating application is the 3-D reconstruction of viruses based on solution x-ray scattering data. The object model includes symmetry, positivity and support constraints and has the form of a truncated orthonormal expansion and the parameters are estimated by maximum likelihood methods. Successful 3-D reconstructions based on synthetic and experimental measurements from Cowpea mosaic virus are described.

**Index Terms**—Fourier transform magnitude, image reconstruction, virus, x-ray scattering.

## I. INTRODUCTION

IN THIS paper we describe object models and algorithms for the three-dimensional (3-D) reconstruction of objects based on measurements of the spherical average of the magnitude-squared of the Fourier transform of the object. The motivating application is the 3-D reconstruction of viruses based on x-ray scattering from solutions of the virus particles in which case the object is the electron density in the virus particle. Averaged Fourier transform magnitude measurements also occur in fiber diffraction problems [1], though the averaging is cylindrical rather than spherical, and similar ideas can be used for those problems.

The amount of information in the solution x-ray scattering data is limited. In particular, because of the spherical averaging, the data is one-dimensional (1-D) even though the goal is a 3-D reconstruction. In addition, the data is a strongly nonlinear function of the structure of the virus particle. In spite of these problems, solution x-ray scattering experiments are of interest for several reasons: first, crystallization of a virus is difficult and may, for a particular virus, be impossible. Second, the structures resulting from solution x-ray scattering data will be useful as starting points for reconstructions of high-resolution structures from high-resolution crystal x-ray diffraction data. Third, solution x-ray scattering, unlike single-

crystal x-ray diffraction or cryo-electron microscopy, can study the dynamics of viruses, e.g., the disassembly of the virus particle during the process of infecting a new host cell. In particular, the recent availability of intense synchrotron sources and sensitive low-angle x-ray detectors makes it possible to collect a complete data set in a time on the order of 100 ms and from sequences of such data sets it is then possible and of great interest to compute a motion picture of the virus dynamics.

There is a tremendous range of virus structures. This paper considers the so-called “spherical viruses” which are viruses with a shell of protein (the so-called “capsid”) surrounding an inner core of nucleic acid. The diameter of the entire particle is  $10^2$ – $10^3$  Å. The capsid is “crystalline” in the sense that it is constructed from many repetitions of the same polypeptides and the entire capsid is invariant under the rotational symmetries of the icosahedron.

Because of the limited amount of data, only low resolution reconstructions can be achieved and use of all available *a priori* knowledge about the particle is crucial. We approach this reconstruction problem by proposing a low-resolution parameterized model of the particle, combining this model with the physics of the measurement, and solving a parameter estimation problem.

Most current algorithms for 3-D reconstruction from solution x-ray scattering data produce reconstructions that have only radial and no angular dependence for the electron density function [2], [3]. This was a reasonable approximation when the reconstruction is done using presynchrotron data but now can be improved on. Another approach [4] includes angular dependence but has a limited type of radial dependence: the electron density is assumed to be piecewise constant with two regions, core and capsid, and the reconstruction problem then amounts to determining the surface between the core and inner edge of the capsid and the surface bounding the outer edge of the capsid. Our goal in the present paper is to compute reconstructions in which there is arbitrary radial and angular dependence.

The remainder of this paper is organized in the following fashion. The physics of the scattering and the model of the virus are described in Sections II and III, respectively, and ambiguities in estimating the parameters of the particle model from the solution x-ray scattering data are discussed in Section IV. The statistical model of the measurement process and maximum likelihood estimation of the parameters in the virus model is described in Section V. Numerical results on synthetic and experimental data from Cowpea mosaic virus

Manuscript received July 16, 1996; revised January 12, 1998. This work was supported by a Purdue Research Foundation Research Grant and by the National Science Foundation under Grants BIR-9513594 and DBI-9630497. The associate editor coordinating the review of this manuscript and approving it for publication was Prof. Hua Lee.

Y. Zheng was with the School of Electrical and Computer Engineering, Purdue University, West Lafayette, IN 47907-1285 USA. He is now with GE Corporate Research and Development, Schenectady, NY 12301 USA.

P. C. Doerschuk is with the School of Electrical and Computer Engineering, Purdue University, West Lafayette, IN 47907-1285 USA (e-mail: doerschu@ecn.purdue.edu).

Publisher Item Identifier S 1057-7149(98)07753-7.

are described in Section VI and the models, algorithms, and results are discussed in Section VII.

## II. THE SCATTERING MODEL

Because the particles in the solution are randomly positioned and randomly rotated, the standard model [5] for the solution x-ray scattering is that the measured intensity is the spherical average of the magnitude-squared of the Fourier transform of the electron density in one particle. Let the electron density in one particle, its Fourier transform, and the measured intensity be denoted by  $\rho(\mathbf{x})$ ,  $P(\mathbf{k})$ , and  $I(k)$ , respectively. Without additional complication,  $\rho(\mathbf{x})$  can be complex. Then the standard model is

$$P(\mathbf{k}) = \frac{1}{(2\pi)^{3/2}} \int \rho(\mathbf{x}) \exp(-i\mathbf{k}^T \mathbf{x}) d^3\mathbf{x} \quad (1)$$

$$I(k) = \frac{1}{4\pi} \int |P(\mathbf{k})|^2 d\Omega' \quad (2)$$

where  $\int d\Omega'$  denotes integration over solid angles in Fourier space [ $\mathbf{k} = (k, \theta', \phi')$ ] which, in spherical coordinates, is  $\int_{\phi'=0}^{2\pi} \int_{\theta'=0}^{\pi} \sin \theta' d\theta' d\phi'$ . Notice that the data,  $I(k)$ , is one-dimensional.

In order to gain some intuition about the solution x-ray scattering data, it is worthwhile to consider a crude model of a virus in which the virus is a solid sphere of radius  $\xi_0$  and electron density  $\rho_0$ . The solution x-ray scattering pattern from such a particle, denoted by  $I_0(k)$ , is  $I_0(k) = (2/\pi) [\rho_0 \xi_0^3 j_1(k\xi_0)/(k\xi_0)]^2$  where  $j_l$  is the  $l$ th order spherical Bessel function of the first kind [6, Eq. 16.9], and the envelope of its asymptotic behavior, denoted by  $\bar{I}_0(k)$ , is

$$\bar{I}_0(k) = \frac{2}{\pi} [\rho_0 \xi_0^3 / (k\xi_0)^2]^2. \quad (3)$$

Therefore, the fundamental behavior of  $I(k)$  is to decline as  $1/k^4$ .

## III. THE PARTICLE MODEL

The particle has three characteristics that we wish to incorporate into the model.

- 1) Icosahedral constraint:  $\rho$  has icosahedral symmetry, that is,  $\rho(\mathbf{R}_\beta^{-1}\mathbf{x}) = \rho(\mathbf{x})$  for all  $\mathbf{x} \in \mathcal{R}^3$  ( $\mathcal{R}$  are the real numbers) and  $\beta = 0, \dots, 59$  where  $\mathbf{R}_\beta \in \mathcal{R}^{3 \times 3}$  is the orthonormal matrix representing the  $\beta$ th rotation of the icosahedral group [7], [8]. The icosahedron (Fig. 1) is constructed from 20 equilateral triangles and has three types of symmetries: fivefold axes where five triangles meet, threefold axes through the center of each triangle, and twofold axes at the midpoint of each edge between two triangles.
- 2) Support constraint:  $\rho(\mathbf{x}) = 0$  for  $|\mathbf{x}| \leq R_-$  and  $|\mathbf{x}| \geq R_+$ .
- 3) Positivity constraint:  $\rho(\mathbf{x}) \geq 0$  for all  $\mathbf{x} \in \mathcal{R}^3$ .

In addition, it is desirable to analytically compute  $P(\mathbf{k})$  from  $\rho(\mathbf{x})$  and  $I(k)$  from  $P(\mathbf{k})$  since these are 3-D and 2-D integrals, respectively.

Because of the spherical averaging in the measurement process, the icosahedral symmetry (a rotational symmetry),

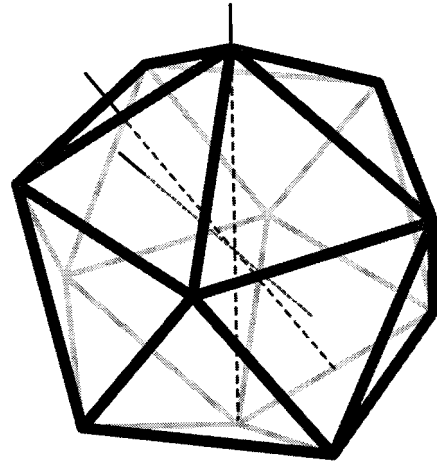


Fig. 1. Icosahedron. One symmetry axis of each type—two-, three-, and fivefold—is shown.

and the minimum and maximum radii for the region in which  $\rho(\mathbf{x})$  may be nonzero, it is natural to use spherical coordinates in both object [ $\mathbf{x} = (r, \theta, \phi)$ ] and Fourier spaces [ $\mathbf{k} = (k, \theta', \phi')$ ]. In order to easily compute the Fourier transform relating  $\rho(\mathbf{x})$  to  $P(\mathbf{k})$ , it is natural to describe  $\rho(\mathbf{x})$  as an orthonormal expansion where the angular functions are harmonic. We first discuss the angular functions and then the radial functions.

### A. Angular Functions

Because of the icosahedral constraint, a natural approach for the angular functions is to use icosahedral harmonics [5], [9]–[12], which are denoted by  $T_{l,n}(\theta, \phi)$ . The two key properties of the  $T_{l,n}$  functions are that every weighted sum of  $T_{l,n}$  functions is a function that has icosahedral symmetry and every smooth icosahedrally symmetric function can be expanded as a weighted sum of  $T_{l,n}$  functions. It is standard to require the additional properties that the  $T_{l,n}$  functions are real valued and orthonormal. An example  $T_{l,n}$  function is shown in Fig. 2. The standard approach to icosahedral harmonics is to describe them as a linear combination of spherical harmonics [denoted by  $Y_{l,m}(\theta, \phi)$ ],

$$T_{l,n}(\theta, \phi) = \sum_{m=-l}^{+l} b_{l,n,m} Y_{l,m}(\theta, \phi) \quad (4)$$

in which case the key is to determine the  $b_{l,n,m}$  coefficients. For the values of  $l$  used in this paper, the values of the  $b_{l,n,m}$  coefficients are known [5], [9]. Using new methods [7], [8], we have, however, extended this work and determined explicit exact values for the  $b_{l,n,m}$  coefficients for arbitrary indices.

Let  $\rho(\mathbf{x})$  be real and icosahedrally symmetric. Then the expansion of  $\rho(\mathbf{x})$  in icosahedral harmonics and the solution x-ray scattering  $I(k)$  due to  $\rho(\mathbf{x})$  are

$$\rho(r, \theta, \phi) = \sum_{l=0}^{\infty} \sum_{n=0}^{N_l-1} A_{l,n}(r) T_{l,n}(\theta, \phi) \quad (5)$$

$$I(k) = \frac{1}{4\pi} \sum_{l=0}^{\infty} \sum_{n=0}^{N_l-1} a_{l,n}^2(k) \quad (6)$$



Fig. 2. Surface plot of icosahedral harmonic  $T_{10,0}(\theta, \phi) = 896\,313\,600P_{10,0}(\cos\theta) + 27\,360P_{10,5}(\cos\theta)\cos 5\phi + P_{10,10}(\cos\theta)\cos 10\phi$ .

where  $A_{l,n}(r) = \int \rho(r, \theta, \phi) T_{l,n}(\theta, \phi) d\Omega$  are real since  $\rho(r, \theta, \phi)$  and  $T_{l,n}(\theta, \phi)$  are real and where  $a_{l,m}(k)$  is the spherical Hankel transform<sup>1</sup> of  $A_{l,m}(r)$ , i.e.,

$$a_{l,m}(k) = \sqrt{\frac{2}{\pi}} \int_0^\infty A_{l,m}(r) j_l(kr) r^2 dr. \quad (7)$$

Note that the finite  $n$  sum in (5) is not due to truncation for practical numerical reasons but rather due to the finite number of icosahedral harmonics of order  $l$ . Any choice of weights in (5) leads to a  $\rho(r, \theta, \phi)$  which exhibits the icosahedral symmetry, i.e., the weights are unconstrained, and for any smooth icosahedrally symmetric  $\rho(\mathbf{x})$  there exists a set of weights such that  $\rho(\mathbf{x})$  can be expressed according to (5).

Not only does use of the  $T_{l,n}(\theta, \phi)$  allow the weights  $A_{l,n}(r)$  to be unconstrained and real, but it also dramatically reduces the number of weights that must be estimated from the data. For a particular order  $l$ , let  $N_l$  be the number of icosahedral harmonics and  $M_l = 2l + 1$  be the number of spherical harmonics. First,  $N_l = 0$  for  $l \in \{1-5, 7-9, 11, 13, 14, 17, 19, 23, 29\}$ , i.e., for these values of  $l$  there are no icosahedral harmonics and so the corresponding weights drop out of the problem. Second, for any  $l$ ,  $N_l$  is dramatically smaller than  $M_l$  [10]. For example, the number of linearly independent spherical harmonics with  $l < 30$  is 900, whereas the corresponding number of linearly independent icosahedral harmonics is just 15, a reduction by a factor of 60, which is the number of symmetry elements in the icosahedral group.

### B. Radial Functions

We now describe the radial functions used for the expansion of  $A_{l,n}(r)$ . Because the spherical Hankel transform depends on  $l$ , it is convenient to use different sets of basis functions for different values of  $l$ . The basis functions and weights are denoted by  $H_{l,p}(r)$  and  $c_{l,n,p}$ , respectively, so that  $A_{l,n}(r) =$

<sup>1</sup>Let  $U_\nu(z)$  be a cylindrical Bessel function. Since the corresponding spherical Bessel function  $u_\nu(z)$  is defined by  $u_\nu(z) = (\pi/(2z))^{1/2} U_{\nu+1/2}(z)$ , the spherical Hankel transform can easily be derived from the standard cylindrical Hankel transform [13, p. 944, Eqs. 8.3.64 and 8.3.65].

$\sum_p c_{l,n,p} H_{l,p}(r)$ ,  $a_{l,n}(k) = \sum_p c_{l,n,p} h_{l,p}(k)$ , and

$$I(k) = \frac{1}{4\pi} \sum_{l=0}^\infty \sum_{n=0}^{N_l-1} \left[ \sum_p c_{l,n,p} h_{l,p}(k) \right]^2 \quad (8)$$

where  $h_{l,p}(k)$  is the spherical Hankel transform of  $H_{l,p}(r)$ . From Parseval's relation for spherical Hankel transforms it follows that orthonormality of  $H_{l,p}(r)$  for fixed  $l$ , i.e.,  $\int_0^\infty H_{l,p}(r) H_{l,p'}^*(r) r^2 dr = \delta_{p,p'}$ , implies the same orthonormality of  $h_{l,p}(k)$  for fixed  $l$ . The functions  $H_{l,p}(r)$  must be selected to achieve three goals, as follows.

- 1)  $H_{l,p}(r) = 0$  for  $r \leq R_-$  and  $r \geq R_+$ , since this condition is equivalent to the support constraint.
- 2) The functions  $H_{l,p}(r)$  are orthonormal for fixed  $l$  since orthonormality will lead to superior behavior in the numerical algorithms.
- 3) The spherical Hankel transform of  $H_{l,p}(r)$  can be efficiently computed since this is equivalent to efficiently computing the 3-D Fourier transform  $P(\mathbf{k})$  of  $\rho(\mathbf{x})$ .

One method to achieve all three objectives, including analytical rather than only efficient computation of the spherical Hankel transform of  $H_{l,p}(r)$ , is to define  $H_{l,p}(r)$  to be certain linear combinations of spherical Bessel functions of order  $l$  which can be shown to achieve Goals 1 and 2 based on Sturm–Liouville theory [14, ch. 7]. Note that the behavior of  $h_{l,p}(k)$  plays an important role in experiment design because it is necessary to determine which  $(l, p)$  contribute to the measured data over what range of  $k$ . For instance,  $h_{l,p}(k) \approx 0$  until  $k \approx 0.1l$ .

### C. Summary

The representation of  $\rho(\mathbf{x})$  by icosahedral harmonics  $T_{l,n}(\theta, \phi)$  and radial functions  $H_{l,p}(r)$ , i.e.,

$$\rho(\mathbf{x}) = \sum_{l=0}^\infty \sum_{n=0}^{N_l-1} \sum_{p=1}^\infty c_{l,n,p} H_{l,p}(r) T_{l,n}(\theta, \phi) \quad (9)$$

gives a one-to-one correspondence between sets of  $c_{l,n,p}$  coefficients and functions  $\rho(\mathbf{x})$  that satisfy the icosahedral and support constraints. Furthermore, it is easy to compute the solution x-ray scattering intensity (8). The only constraint on  $\rho(\mathbf{x})$  that is not incorporated is the positivity constraint, which is discussed in Section V-B.

## IV. UNIQUENESS

An important question is whether the measurement of  $I(k)$  for the idealized range  $0 \leq k < \infty$  determines a unique  $\rho(\mathbf{x})$  or whether many different  $\rho(\mathbf{x})$  lead to the same  $I(k)$ . This is a complicated question because of the nonlinear nature of the measurement process and because of the modeling restrictions that are imposed on  $\rho(\mathbf{x})$ .

Consider  $\rho(\mathbf{x})$  satisfying the icosahedral constraint. Then, without loss of generality,  $\rho(\mathbf{x})$  can be represented by a weighted sum of icosahedral harmonics (5) where the  $A_{l,n}(r)$  functions are unconstrained. Addition of the support constraint on  $\rho(\mathbf{x})$  is equivalent to a support constraint on  $A_{l,n}(r)$ , specifically,  $A_{l,n}(r) = 0$  for  $0 \leq r \leq R_-$  and  $r \geq R_+$  and

for all  $l$  and  $n$ . In either case, the key result is that orthogonal linear combinations in  $n$  for fixed  $l$  of the  $A_{l,n}(r)$  functions lead to identical  $I(k)$ . More specifically, let  $\mathbf{Q}_l \in \mathcal{R}^{N_l \times N_l}$  be an orthogonal matrix with elements  $q_{l,n,n'}$ . Then, because the spherical Hankel transform depends on  $l$  but not on  $n$  and because  $\mathbf{Q}_l$  is independent of  $r$ , it can be shown that the solution scattering of a structure  $\rho(\mathbf{x})$  with weights  $A_{l,n}(r)$  is identical to the solution scattering of a structure  $\rho'(\mathbf{x})$  with weights  $A'_{l,n}(r) = \sum_{n'=0}^{N_l-1} q_{l,n,n'} A_{l,n'}(r)$ . Therefore, the weights cannot be uniquely reconstructed from the solution x-ray scattering data.

Now assume that  $\rho(\mathbf{x})$  also satisfies the positivity constraint. Then it is important, but difficult, to determine whether  $\rho'(\mathbf{x})$  will satisfy the positivity constraint as a function of the choice of  $\mathbf{Q}_l$ . Both situations occur. For instance,  $\mathbf{Q}_l = -I_{N_l}$  ( $I_n$  is the  $n \times n$  identity matrix) leads to  $\rho'(\mathbf{x}) = -\rho(\mathbf{x})$  which obviously disobeys the constraint. However,  $\mathbf{Q}_l = (-1)^l I_{N_l}$  leads to  $\rho'(\mathbf{x}) = \rho(-\mathbf{x})$  (inversion through the origin, which is not in the icosahedral group) which obviously obeys the constraint. More generally, the choice of  $\mathbf{Q}_l$  interacts with the details of  $\rho(\mathbf{x})$  [i.e., the details of  $A_{l,n}(r)$ ] to determine whether  $\rho'(\mathbf{x})$  will satisfy the constraint and we are unable to make further analytical statements.

In the presence of icosahedral symmetry, this ambiguity is actually not as great as it seems. If  $N_l = 1$  then  $\mathbf{Q}_l = \pm 1$ . Furthermore (Section III-A),  $N_l = 0$  or  $1$  for  $l < 30$  and  $N_l = 0$  fifteen times. Therefore, reconstructions including all harmonics up through  $l = 29$  can be computed with only  $2^{15}$  discrete ambiguities of which  $2^{14}$  are related to the second  $2^{14}$  by inversion through the origin ( $\rho_1(\mathbf{x}) = \rho_2(-\mathbf{x})$ ). In the absence of icosahedral symmetry, then  $N_l$  is replaced by  $M_l$  and  $M_l = 2l + 1 > 1$  for all  $l > 0$  so the ambiguity is great even for low  $l$  reconstructions. In the presence of icosahedral symmetry, an additional qualitative statement can be made. Assume that the series is truncated at  $l < 30$  so the  $\mathbf{Q}_l = \pm 1$ . Because  $T_{0,0}(\theta, \phi) = Y_{0,0}(\theta, \phi) = 1/\sqrt{4\pi} > 0$  for all values of  $\theta$  and  $\phi$ , it is possible to have  $A_{0,0}(r)$  sufficiently larger than  $A_{l,n}(r)$  for  $l > 0$  such that all choices of  $\mathbf{Q}_l$  for  $1 \leq l < 30$  lead to  $\rho(\mathbf{x})$  which do not violate the positivity constraint. Only  $A_{0,0}(r)$  can dominate the problem in this sense because of all the  $T_{l,n}(\theta, \phi)$ , only  $T_{0,0}(\theta, \phi)$  is positive for all values of  $\theta$  and  $\phi$ .

Motivated by the isomorphous replacement method [1] of macromolecular single-crystal x-ray diffraction, we propose a novel experiment which we show (Section VI) results in data from which the  $\mathbf{Q}_l$  matrices can be estimated. Isomorphous replacement involves comparing several diffraction patterns. One pattern is from a crystal made from the molecule of interest and the additional patterns are from crystals made from chemical derivatives of the molecule of interest where the derivatives are the addition of heavy metal atoms which have many electrons and therefore are strong scatterers and which, ideally, do not alter the 3-D structure of the molecule. We propose to use the same approach in solution x-ray scattering. In the single-crystal diffraction case, the number of electrons that can be added by making a derivative is limited to the number of electrons in a heavy metal atom because the goal is an atomic-resolution structure so the additional

electrons must be confined to an atomic-sized volume. In the solution scattering case, the resolution goals are much lower so the volume containing the added electrons can be much larger and therefore the number of electrons added can be much greater. For instance, in cryo-electron microscopy, calculations have been done where the added electrons take the form of an antibody fragment (e.g., [15]). Experimental techniques for adding organo-metallic gold clusters have also been developed [16].

Let  $\rho(\mathbf{x})$  and  $\rho'(\mathbf{x})$  be the electron density in the original virus and the modified viruses, respectively. Then, because the modification does not deform the virus but rather adds an additional icosahedrally symmetric impulse of charge,  $\rho'(r, \theta, \phi) = \rho(r, \theta, \phi) + Q\Delta(\theta, \phi; \theta_0, \phi_0)\delta(r - r_0)/r^2$  where  $\mathbf{x}_0 = (r_0, \theta_0, \phi_0)$  is the location (initially unknown) of the added electrons in one asymmetric unit of the icosahedral group,  $Q$  is the amount of added charge,  $\Delta(\theta, \phi; \theta_0, \phi_0)$  is an icosahedrally-symmetric delta function [7], and  $\delta(\cdot)$  is the usual delta function. In the following equations, primed and unprimed variables refer to the modified and unmodified virus, respectively. It is straightforward to compute that  $A'_{l,n}(r) = A_{l,n}(r) + QT_{l,n}(\theta_0, \phi_0)\delta(r - r_0)/r^2$  and  $c'_{l,n,p} = c_{l,n,p} + Q\zeta_{l,n,p}(\mathbf{x}_0)$  where  $\zeta_{l,n,p}(\mathbf{x}_0) = T_{l,n}(\theta_0, \phi_0)H_{l,p}(r_0)/n_{l,p}$ .

## V. STATISTICAL ESTIMATION

### A. Measurement Model

Let  $\mathbf{c}$  denote the set of unknown parameters  $c_{l,n,p}$ . Let  $\hat{I}(k; \mathbf{c})$  denote the solution x-ray scattering which would result from a particle with parameters  $\mathbf{c}$  [(8) with the notation  $I(k)$  replaced by the notation  $\hat{I}(k; \mathbf{c})$  in order to emphasize that this is the predicted value of the solution x-ray scattering if the particle had parameters  $\mathbf{c}$ ]. Let the measurements be taken at  $k = k_j$  for  $j = 1, \dots, J$ .

There are two sources of uncertainty in the measurements. The Poisson counting statistics of the photon arrivals and instrumentation errors including errors such as fluctuation in beam intensity and photon energy. In addition, the failure of the standard model described in (1) and (2) to accurately represent the physics of the experiment due, for instance, to correlations between the particle positions and orientations in the solution, can be treated as a third noise source.

The data used in Section VI is from a film detector and so is intensity rather than photon count data. Let  $I_j$  be the intensity measured at scattering angle  $k_j$ . We describe the intensity data with a Gaussian model in which the different measurements ( $I_j$  versus  $I_{j'}$  with  $j \neq j'$ ) are independent. Therefore, the negative log-likelihood function, denoted by  $\chi(\mathbf{c})$ , is

$$\begin{aligned} \chi(\mathbf{c}) &= -\ln p(\{I_j; j = 1, \dots, J\} | \mathbf{c}) \\ &= \frac{1}{2} \sum_{j=1}^J \{[I_j - \hat{I}(k_j; \mathbf{c})]^2 / \sigma_j^2 + \ln[2\pi\sigma_j^2]\}. \end{aligned} \quad (10)$$

There are several sources of information for choosing the variance of the intensity data (i.e.,  $\sigma_j^2$ ). If instrumentation and modeling errors are the dominant errors then, due to lack of detailed information, a natural model is  $I_j = (1 + \xi_j w_j) \hat{I}(k_j; \mathbf{c})$

where  $w_j$  are zero-mean unit-variance independent Gaussian random variables and  $\xi_j$  are a sequence of known fractional errors. Such a model implies  $\sigma_j^2 = \xi_j^2 \hat{I}^2(k_j; \mathbf{c})$ . If counting statistics are the dominant error source and  $\epsilon$  is the photon energy, then  $\hat{I}(k_j; \mathbf{c})/\epsilon$  is the rate for the Poisson distribution on the number of photons that arrive in an infinitesimal region around  $k_j$ . In the central limit theorem approximation, such a model implies  $\sigma_j^2 = \epsilon \hat{I}(k_j; \mathbf{c})$ . (Recall that  $\sigma_j^2$  is the variance on the intensity data not on the photon count data and the intensity is  $\epsilon$  times the photon count.) As shown in Section VI-C, the range of  $I_j$  is roughly  $10^4$  so the counting statistics cannot be the dominant source of error over the entire range of  $k$  and, in a large part of the range of  $k$ , the rate is sufficiently large such that the central limit theorem approximation is excellent. Independent of the origin of the formula for the variance  $\sigma_j^2$ , it is natural to replace  $\hat{I}(k_j; \mathbf{c})$  in the variance formula by the envelope of the spherical particle scattering intensity (3) in order to simplify the numerical computations. This indicates that  $\sigma_j^2 \sim 1/k_j^\alpha$  with  $4 \leq \alpha \leq 8$  and in Section VI numerical experiments are described with a variety of choices for  $\sigma_j^2$ .

When two solution x-ray scattering patterns are measured, one from the virus and one from a derivative of the virus, the basic assumption is that the two sets of measurements are independent so that the negative log-likelihoods add. (Use of multiple derivatives is a straightforward generalization.) Let  $\zeta(\mathbf{x}_0)$  denote the entire collection of  $\zeta_{l,n,p}(\mathbf{x}_0)$ . The unknown parameters are  $\mathbf{c}$  and  $\mathbf{x}_0$ . The number of additional electrons, i.e.,  $Q$ , is known from chemical methods. The negative log-likelihood is

$$\chi'(\mathbf{c}, \mathbf{x}_0) = \chi(\mathbf{c}) + \chi(\mathbf{c} + Q\zeta(\mathbf{x}_0)). \quad (11)$$

### B. A Priori Model

The purpose of an *a priori* probability distribution on the unknown parameters  $\mathbf{c}$  would be to include constraints on  $\rho(\mathbf{x})$ . Two of the constraints (icosahedral and support constraints) are built into the  $\mathbf{c}$  parameters and therefore for these constraints there is no need for an *a priori* distribution. However, the positivity constraint has not yet been addressed. The ability to achieve a positivity constraint is lost when the orthonormal expansion of  $\rho(\mathbf{x})$  is truncated to a finite  $l$ . Specifically, unless  $A_{0,0}(r)$  is positive for all  $r$  and dominates the other terms as described in Section IV,  $\rho(\mathbf{x})$  is guaranteed to ring and go negative. While the positivity constraint could be weakened to a negativity penalty, which could be described as an *a priori* distribution, we have found in numerical work that this is not necessary (see Section VI).

However, an *a priori* model is still useful for the following reason. It is difficult to know how to truncate the  $l$  and  $p$  sums for a given set of data. In particular, if excessively large  $l$  or  $p$  are allowed, then  $h_{l,p}(k)$  is essentially zero [or equal to some other  $h_{l',p'}(k)$  function] throughout the range of  $k$  for which data is available and the corresponding  $c_{l,n,p}$  coefficients are essentially unconstrained (or indeterminate) and have a tendency to grow large instead of go to zero. This problem can be resolved by using an *a priori* model in which the  $c_{l,n,p}$  are independent and Gaussian with zero mean and

variance  $1/\sqrt{\lambda}$  where  $\lambda$  is an empirical parameter. Use of this model results in the addition of the term

$$\chi_\lambda(\mathbf{c}) = \frac{\lambda}{2} \sum_{l=0}^{\infty} \sum_{n=0}^{N_l-1} \sum_{p=1}^{\infty} c_{l,n,p}^2 \quad (12)$$

to the negative log-likelihood function.

The term  $\chi_\lambda(\mathbf{c})$  could also be described as an energy penalty that helps to regularize the problem. An additional type of penalty, which has not been previously discussed but which is often used for regularization purposes, is a roughness penalty on  $\rho(\mathbf{x})$ . Such a penalty is fundamentally already built into the  $\mathbf{c}$  parameters because roughness is controlled by the maximum  $l$  and  $p$  that is included in the truncated orthonormal expansion for  $\rho(\mathbf{x})$ . Therefore, a separate roughness penalty, which could be described as an *a priori* distribution, is not necessary.

### C. Estimation Criterion and Numerical Methods

The unknown parameters  $\mathbf{c}$  or  $(\mathbf{c}, \mathbf{x}_0)$  are estimated by maximum likelihood or, with  $\lambda \neq 0$ , maximum *a posteriori* methods. This requires the numerical minimization of the negative log-likelihood function. If only a scattering pattern from the virus is measured, then the cost criterion to be minimized is  $\chi(\mathbf{c}) + \chi_\lambda(\mathbf{c})$  [(10) and (12)] which is a nonlinear least squares cost criterion. Therefore, the minimum is located by the Levenberg–Marquardt method with analytical gradients [17, pp. 683–688]. Computation of  $\hat{I}(k_j; \mathbf{c})$  and  $\partial \hat{I}(k_j; \mathbf{c})/\partial c_{l,n,p}$  is fast once  $h_{l,p}(k)$  has been precomputed at  $k = k_j$  ( $j = 1, \dots, J$ ).

If solution x-ray scattering patterns are measured both from the virus and from a derivative of the virus, then it is possible to directly minimize  $\chi(\mathbf{c}) + \chi(\mathbf{c} + Q\zeta(\mathbf{x}_0)) + \chi_\lambda(\mathbf{c})$  jointly with respect to  $\mathbf{c}$  and  $\mathbf{x}_0$  but we have instead used a two step procedure: minimization of  $\chi(\mathbf{c}) + \chi_\lambda(\mathbf{c})$  with respect to  $\mathbf{c}$ , giving a result denoted by  $\mathbf{c}^*$ , followed by minimization of  $\chi(\mathbf{c}^* + Q\zeta(\mathbf{x}_0))$  with respect to  $\mathbf{x}_0$  and the possible  $Q_l$  matrices, i.e., the possible signs on the  $\mathbf{c}^*$  coefficients. More precisely, the second step is a set of minimizations: choose a set of signs for the  $\mathbf{c}^*$  coefficients, denote the signed coefficients by  $\mathbf{d}$ , and minimize  $\chi(\mathbf{d} + Q\zeta(\mathbf{x}_0))$  with respect to  $\mathbf{x}_0$ . As a final estimate of  $\mathbf{c}$  take that  $\mathbf{d}$  which lead to the minimum value for  $\min_{\mathbf{x}_0} \chi(\mathbf{d} + Q\zeta(\mathbf{x}_0))$ . If desired, the corresponding estimate of  $\mathbf{x}_0$  is also available. The two step approach is motivated by the following observations: first, the optimizations are simplified, in particular, the nonlinear least squares problem of optimizing  $\chi(\mathbf{c}) + \chi_\lambda(\mathbf{c})$  is preserved. Second, in single-crystal x-ray diffraction it is often the case that nonidealities are much more severe in the data from the modified molecule and we expect that the same would occur in the solution x-ray scattering. Therefore, determining the absolute values of the  $\mathbf{c}$  components based on the data from the unmodified particle may yield superior performance.

## VI. NUMERICAL RESULTS

We consider data from Cowpea mosaic virus (CpMV), which is a virus whose structure has been solved at atomic levels of resolution by single-crystal x-ray diffraction studies

[18] and which contains  $60 \times 4341$  nonhydrogen atoms and measures approximately  $160 \text{ \AA}$  in radius.

The  $l$  and  $p$  sums are truncated to  $L$  and  $P$ , respectively.  $L$  is determined from the number of zero-crossings around any great circle and from comparing the  $h_{l,p}(k)$  plots with the  $k$ -range of the available data.  $P$  is determined from the number of zero-crossings between  $R_-$  and  $R_+$  and from comparing the  $h_{l,p}(k)$  plots with the  $k$ -range of the available data.

The values of  $R_+$  and  $R_-$  in the  $H_{l,p}(r)$  functions are determined by first fitting a spherical shell model [4] to the data. If these values appear to be incorrect [e.g., high values of  $\rho(\mathbf{x})$  occur near the edge of the region of support in the reconstructed object], then they are altered manually guided by  $\min_{\mathbf{c}} \chi(\mathbf{c}) + \chi_{\lambda}(\mathbf{c})$ . In the numerical results described in this section,  $R_- = 95 \text{ \AA}$  and  $R_+ = 160 \text{ \AA}$ .

The initial conditions on  $\mathbf{c}$  are independent random variables uniformly distributed on  $[0, 1]$ . Restarting from roughly 10 such initial conditions is sufficient to reach the global minimum.

We discuss several different sets of  $\rho(\mathbf{x})$ ,  $A_{l,n}(r)$ ,  $c_{l,n,p}$ , and  $I(k)$  variables. The first set, which exactly represent the atomic resolution structure, contains variables which are denoted by  $\rho^{(a)}(\mathbf{x})$ ,  $A_{l,n}^{(a)}(r)$ ,  $c_{l,n,p}^{(a)}$ , and  $I^{(a)}(k)$  (superscript “ $a$ ” for “atomic”) and can be computed from the atomic resolution structure starting with the definition

$$\rho^{(a)}(\mathbf{x}) = \sum_{\mu=1}^M \sum_{\beta=0}^{59} f_{\mu} \delta(\mathbf{x} - \mathbf{R}_{\beta} \mathbf{x}_{\mu}) \quad (13)$$

where  $M$  is the number of atoms in the asymmetric unit of the icosahedral group,  $\mathbf{x}_{\mu} = (r_{\mu}, \theta_{\mu}, \phi_{\mu})$  is the location of the  $\mu$ th atom,  $f_{\mu}$  is the atomic scattering factor of the  $\mu$ th atom, and  $\mathbf{R}_{\beta}$  are the rotations of the icosahedral group. Because  $\rho^{(a)}(\mathbf{x})$  and  $A_{l,n}^{(a)}(r)$  are impulsive, it is difficult to compare them with the nonimpulsive low-resolution results of the estimation process. Therefore, we define lowpass versions of  $\rho^{(a)}(\mathbf{x})$  and  $A_{l,n}^{(a)}(r)$ , which are denoted by  $\rho^{\text{LP}}(\mathbf{x})$  and  $A_{l,n}^{\text{LP}}(r)$ , by replacing the 3-D delta function in  $\rho^{(a)}(\mathbf{x})$  by  $(1/\sqrt{2\pi R}) \exp(-|\cdot|^2/(2R^2))$  and the 1-D delta function in  $A_{l,n}^{(a)}(r)$  by  $(u(\cdot+R) - u(\cdot-R))/(2R)$  where  $u(\cdot)$  is the unit step function and  $R = 5 \text{ \AA}$ .

The second set, which are derived from the atomic resolution structure by truncation of the  $l$  and  $p$  sums, contains variables which are denoted by  $\rho^{(\eta)}(\mathbf{x})$ ,  $A_{l,n}^{(\eta)}(r)$ ,  $c_{l,n,p}^{(\eta)}$ , and  $I^{(\eta)}(k)$  and can be computed from the atomic resolution structure starting from the definition

$$c_{l,n,p}^{(\eta)} = \begin{cases} c_{l,n,p}^{(a)}, & p \leq P_{l,n}^{(\eta)} \text{ and } l \leq L^{(\eta)} \\ 0, & \text{otherwise.} \end{cases} \quad (14)$$

We consider three different truncations which are labeled  $\eta = 22, 12, 12^-$  and are defined as follows: for  $\eta = 22$  the limits are  $L = 22$  and  $P_{l,n} = 10$  which leads to 100  $c_{l,n,p}$  parameters since there are no icosahedral harmonics for  $l \in \{1-5, 7-9, 11, 13, 14, 17, 19, 23, 29\}$ . For  $\eta = 12$  the limits are  $L = 12$ ,  $P_{0,0} = 4$ , and  $P_{6,0} = P_{10,0} = P_{12,0} = 3$ . Finally, for  $\eta = 12^-$  the limits are  $L = 12$ ,  $P_{0,0} = 3$ , and  $P_{6,0} = P_{10,0} = P_{12,0} = 2$ .

The third set, which is preprocessed experimental data [2], includes only a x-ray solution scattering intensity which is denoted by  $I^{(e)}(k)$ . The preprocessing is removal of the background. Specifically, a continuous piecewise linear function with slope discontinuities at the 6 minima of the experimental data is interpolated through the six minima. Then this function is subtracted from the experimental data to yield  $I^{(e)}(k)$ . Since  $I^{(e)}(k)$  is sampled at intervals of  $1.07 \times 10^{-4} \text{ \AA}^{-1}$ , we use the same interval for  $I^{(\eta)}(k)$  and  $I^{(a)}(k)$ . Since the range of  $k$  for  $I^{(e)}(k)$  is  $k_{\min} \leq k \leq k_{\max}$  where  $k_{\min} = 0.004279 \text{ \AA}^{-1}$  and  $k_{\max} = 0.020853 \text{ \AA}^{-1}$ , we use either  $k_{\min} \leq k \leq k_{\max}$ , representing historical  $k$ -ranges which are achievable with rotating anode x-ray generators and film detectors, or  $k_{\min} \leq k \leq 2k_{\max}$ , representing  $k$ -ranges achievable with modern synchrotrons and detectors.

The fourth set, which are reconstructions computed by the methods described in this paper, contains variables that are denoted by  $\hat{\rho}^{(\eta,I)}(\mathbf{x})$ ,  $\hat{A}_{l,n}^{(\eta,I)}(r)$ ,  $\hat{c}_{l,n,p}^{(\eta,I)}$ , and  $\hat{I}^{(\eta,I)}(k)$  where the label  $\eta$  has the same meaning as above and the label  $I$  describes the data used as the input to the reconstruction:  $I = I^{(\eta)}, I^{(a)}, I^{(e)}$ .

For both  $I^{(\eta)}(k)$  and  $I^{(a)}(k)$ , Gaussian noise has been considered. In particular, the data used by the reconstruction algorithm are  $I(k_j) \max(1 + \xi w_j, 0)$  where  $w_j$  are independent and identically distributed (i.i.d.) Gaussian random variables with mean zero and variance one,  $\xi = 0.05$ , and  $I(k_j)$  is either  $I^{(\eta)}(k_j)$  or  $I^{(a)}(k_j)$ . This value of noise is typical of modern experiments [4].

An important measure of performance is the normalized  $L_2$  norm squared of the difference between the truncated atomic and the estimated electron densities

$$\begin{aligned} \epsilon^{(\eta,I)} &= \int |\rho^{(\eta)}(\mathbf{x}) - \hat{\rho}^{(\eta,I)}(\mathbf{x})|^2 d^3\mathbf{x} / \int |\rho^{(\eta)}(\mathbf{x})|^2 d^3\mathbf{x} \\ &= \sum_{l=0}^{\infty} \sum_{n=0}^{N_l-1} \sum_{p=1}^{\infty} |c_{l,n,p}^{(\eta)} - \hat{c}_{l,n,p}^{(\eta,I)}|^2 / \\ &\quad \sum_{l=0}^{\infty} \sum_{n=0}^{N_l-1} \sum_{p=1}^{\infty} |c_{l,n,p}^{(\eta)}|^2. \end{aligned} \quad (15)$$

#### A. The $I^{(12)}(k)$ Data

In this section, we describe the performance of the estimator on the simulated  $I^{(12)}(k)$  data. Reconstructions based on the  $I^{(12)}(k)$  data are of interest because the model used by the estimator and the model used to generate the data are of the same type. Two situations are investigated: 1) reconstruction from a single scattering pattern (both noise-free and noisy cases) and 2) reconstruction from a pair of scattering patterns where the second pattern is from a labeled derivative of the virus where the location of the label is not known to the estimator (both noise-free and noisy cases).

The reconstructions from a single scattering pattern are presented first. The cost criterion is  $\chi(\mathbf{c}) + \chi_{\lambda}(\mathbf{c})$  with  $\lambda = 1$ . The estimates are not sensitive to the value of  $\lambda$ . The variance is  $1/\sigma_j^2 = k_j^{\alpha}$  with  $\alpha = 4$ . The  $k$ -range is  $k_{\min} \leq k \leq 2k_{\max}$ . Approximately 50 steps of the Levenberg–Marquardt method

TABLE I  
COMPUTED AND ESTIMATED VALUES OF  $c_{l,n,p}$  AND THE RESULTING VALUE OF  $\epsilon$  FOR THE  $I^{(12)}(k)$  SYNTHETIC DATA WITH AND WITHOUT NOISE

$l$	$n$	$p$	$c_{l,n,p}^{(a)}$	$\hat{c}_{l,n,p}^{(12,I^{(12)})}$	
				Noiseless data	Noisy data
0	0	1	9.77753	9.77753	9.7709±0.0319
0	0	2	3.33439	3.33439	3.2936±0.0242
0	0	3	-1.92586	-1.92583	-1.9290±0.1552
0	0	4	-1.58729	-1.58729	-1.4862±0.1726
6	0	1	1.67796	1.67798	1.7158±0.1240
6	0	2	-2.87828	-2.87829	-2.7322±0.1612
6	0	3	0.278339	0.278296	0.3724±0.1953
10	0	1	1.01116	1.01112	1.0972±0.1304
10	0	2	-1.97873	-1.97872	-1.8017±0.3595
10	0	3	-1.4401	-1.44008	-1.0485±0.6254
12	0	1	-0.318764	-0.318735	-0.6791±0.4715
12	0	2	-1.41253	-1.41259	-1.6504±0.4950
12	0	3	0.973701	0.973718	1.1949±0.3698
$\epsilon^{(12,I^{(12)})}$				$7.51 \times 10^{-11}$	$4.71 \times 10^{-3}$ $\pm 1.84 \times 10^{-3}$

were required to minimize the cost criterion. Computed and estimated results for  $c_{l,n,p}$  and values for  $\epsilon$  are contained in Table I. For the noisy case, the results are stated as sample mean plus/minus one sample standard deviation based on 100 independent trials. Since the cost criterion  $\chi(\mathbf{c}) + \chi_\lambda(\mathbf{c})$  is insensitive to the signs of  $c_{l,n,p}$ , the signs were set equal to the signs of  $c_{l,n,p}^{(a)}$  in order that the value of  $\epsilon$  correctly reflect the performance of the estimator. Since the estimated  $c_{l,n,p}$  computed from the noiseless data are essentially perfect, we focus on the estimates from the noisy data. For each of the 100 trials, the scattering  $\hat{I}^{(12,I^{(12)})}(k)$  and the icosahedral harmonics coefficients  $\hat{A}_{l,n}^{(12,I^{(12)})}(r)$  are computed. A plot of  $I^{(12)}(k)$  and the sample mean and sample standard deviation of the 100 trials of  $\hat{I}^{(12,I^{(12)})}(k)$  is shown in Fig. 3. Plots of  $A_{l,n}^{(12)}(r)$  and the sample mean and sample standard deviation of the 100 trials of  $\hat{A}_{l,n}^{(12,I^{(12)})}(r)$  are shown in Fig. 4. Performance of the estimator is good, in spite of the realistic amount of noise corrupting the data.

When two solution x-ray scattering patterns are considered, one from the virus and one from a derivative of the virus, it is possible to determine the signs of the  $c_{l,n,p}$  coefficients. The basic parameters of the problem are the same as for the problem of the previous paragraph. The parameters for the derivative were  $Q = 1000$  and  $\mathbf{x}_0 = (r_0, \theta_0, \phi_0) = (140 \text{ \AA}, \pi/10, \pi/10)$  and the data was computed by replacing  $c_{l,n,p}$  by  $c_{l,n,p} + Q\zeta_{l,n,p}(\mathbf{x}_0)$ . The cost criterion is  $\chi(\mathbf{c}) + \chi_\lambda(\mathbf{c}) + \chi(\mathbf{c} + Q\zeta(\mathbf{x}_0))$ . The two-step optimization procedure described in Section V-C was used. For all numerical simulations with noiseless  $I^{(12)}(k)$  data from the virus and from the derivative of the virus, this method successfully

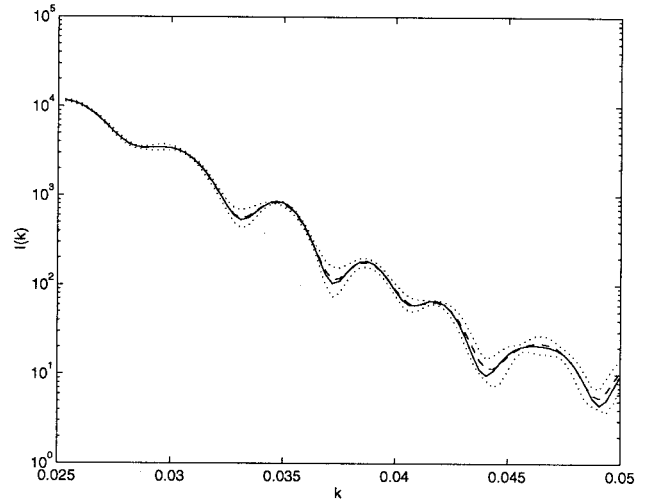


Fig. 3. Solution x-ray scattering data  $I(k)$ :  $I^{(12)}(k)$  (solid curve), sample mean of  $\hat{I}^{(12,I^{(12)})}(k)$  (dashed curve), and sample mean plus/minus one sample standard deviation of  $\hat{I}^{(12,I^{(12)})}(k)$  (two dotted curves). These four curves are essentially indistinguishable for  $k < 0.025 \text{ \AA}^{-1}$  and so that region is not shown.

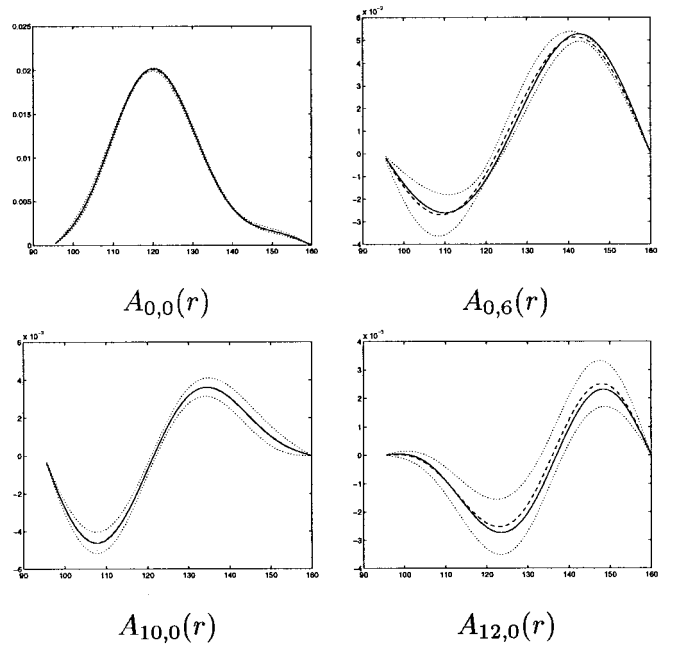


Fig. 4. Icosahedral harmonic expansion coefficients  $A_{l,n}(r)$ :  $A_{l,n}^{(12)}(r)$  (solid curve), sample mean of  $\hat{A}_{l,n}^{(12,I^{(12)})}(r)$  (dashed curve), and sample mean plus/minus one sample standard deviation of  $\hat{A}_{l,n}^{(12,I^{(12)})}(r)$  (two dotted curves).

determines a complete set of correct signs. With noisy data, this method determines a complete set of correct signs in 73 out of 100 simulated data sets. [A complete set contains four signs,  $\pm A_{0,0}(r)$ ,  $\pm A_{6,0}(r)$ ,  $\pm A_{10,0}(r)$ , and  $\pm A_{12,0}(r)$ , though it is obvious without considering a second scattering pattern that the sign of  $A_{0,0}(r)$  must be chosen so that  $A_{0,0}(r)$  is primarily positive.] This process also determines the coordinates of the additional charge  $Q$  in the asymmetric unit of the icosahedron. The true location, as described above,

TABLE II

COMPUTED AND ESTIMATED VALUES FOR  $c_{l,n,p}$ . AS SHOWN IN FIG. 5, THE SOLUTION SCATTERING COMPUTED FROM THE ATOMIC RESOLUTION MODEL ( $I^{(a)}(k)$ ) IS ONLY A MODERATELY GOOD FIT TO THE EXPERIMENTAL SOLUTION SCATTERING DATA ( $I^{(e)}(k)$ ). THEREFORE, IT IS NOT UNEXPECTED THAT THE ESTIMATED  $c_{l,n,p}^{(12^-, I^{(e)})}$  COEFFICIENTS, WHICH ATTEMPT TO FIT THE EXPERIMENTAL  $I^{(e)}(k)$  DATA, DISAGREE TO SOME EXTENT WITH THE COMPUTED  $c_{l,n,p}^{(a)}$  COEFFICIENTS, WHICH ARE COMPUTED FROM THE ATOMIC RESOLUTION MODEL. FOR THE SAME REASON, THE VALUE OF  $\epsilon^{(12^-, I^{(e)})}$ , WHICH IS COMPUTED FROM THE DIFFERENCE  $c_{l,n,p}^{(a)} - c_{l,n,p}^{(12^-, I^{(e)})}$ , IS DIFFICULT TO INTERPRET

$l$	$n$	$p$	$c_{l,n,p}^{(a)}$	$c_{l,n,p}^{(12^-, I^{(e)})}$
0	0	1	9.77753	9.88098
0	0	2	3.33439	3.02935
0	0	3	-1.92586	-2.3585
6	0	1	1.67796	0.97699
6	0	2	-2.87828	-1.2271
10	0	1	1.01116	1.11713
10	0	2	-1.97873	-2.19932
12	0	1	-0.318764	-0.696881
12	0	2	-1.41253	-1.32081
$\epsilon^{(12^-, I^{(e)})}$				0.029

is  $(r_0, \theta_0, \phi_0) = (140 \text{ \AA}, \pi/10, \pi/10)$  while the sample mean plus/minus one sample standard deviation of the estimated locations from the 100 trials is  $(140.5 \pm 4.0345 \text{ \AA}, 0.3890 \pm 0.1904, 0.3255 \pm 0.1103)$ . In spite of the imprecision of the estimated angular position of the added electrons, the method provides moderately accurate signs for the  $A_{l,n}(r)$  functions and thereby removes an otherwise intractable ambiguity from the reconstruction problem.

### B. The $I^{(a)}(k)$ Data

The issue with the  $I^{(a)}(k)$  data is that no model with a finite number of  $c_{l,n,p}$  coefficients or equivalently a finite number of  $A_{l,n}(r)$  weights can exactly represent the data. This is a natural situation in which to investigate the behavior of the estimator as the number of degrees of freedom is increased (i.e., larger  $L$  and  $P$ ) while the amount of data is constant (i.e., constant range for  $k$ ) and also to investigate the effect of the *a priori* model (i.e., the value of  $\lambda$ ). The complete results [19] are summarized here.

The two estimates that are considered are  $\hat{c}_{l,n,p}^{(\eta, I^{(a)})}$  with  $\eta = 12$  and  $\eta = 22$  which have 13 and 100 parameters, respectively. Since there are only 160 data points, 100 is a large number of parameters. The parameters are the same as were used for the  $I^{(12)}(k)$  data, including  $\lambda = 1$ . While  $\eta = 12$  fits the “hidden” variables  $A_{l,n}^{\text{LP}}(r)$  well and  $\rho^{\text{LP}}(\mathbf{x})$  reasonably though with decreased spatial resolution,  $\eta = 12$  does not fit the measurements well at large  $k$ . This might be interpreted as indicating a need for larger  $L$  and  $P$ . However, while  $\eta = 22$  (which has more parameters) fits the measurements very well and  $\rho^{\text{LP}}(\mathbf{x})$  reasonably though with increased artificial spatial resolution,  $\eta = 22$  fits the hidden variables  $A_{l,n}^{\text{LP}}(r)$  poorly. The *a priori* model has a role in this behavior since if

$\lambda = 0$  then the results for  $\eta = 22$  are poorer than for  $\lambda = 1$ . However, the balance between  $\lambda$ ,  $L$ ,  $P$ ,  $k_{\min}$ , and  $k_{\max}$  is difficult to achieve and probably requires interdependencies: most likely  $P$  should be an increasing function of  $l$  so that the maximum angular frequency of a component (controlled by  $l$ ) and the maximum radial frequency (controlled by  $P$ ) increase together. Furthermore, and for the same reason,  $\lambda$  should most likely be a function of  $(l, p)$ , start (i.e.,  $l = p = 0$ ) at a level greater than the  $\lambda = 1$  used here, and be a decreasing function of  $l$ . Finally, as  $k_{\max}$  increases, a higher resolution structure can be computed and therefore  $L$  and  $P$  should increase and  $\lambda$  should decrease.

### B. The $I^{(e)}(k)$ Experimental Data

The  $c_{l,n,p}$  estimates resulting from the minimization of  $\chi(\mathbf{c}) + \chi_\lambda(\mathbf{c})$  with  $\lambda = 1$  and variance  $1/\sigma_j^2 = k_j^\alpha$  with  $\alpha = 4$  using the experimental data  $I^{(e)}(k)$  are shown in Table II. The results are not sensitive to the value of  $\lambda$  or the value of  $\alpha$  in the range  $3 \leq \alpha \leq 8$ . Coefficients for smaller  $l$  are less affected by  $\alpha$  than coefficients for larger  $l$ . The  $k$ -range is  $k_{\min} \leq k \leq k_{\max}$  and, therefore, it is only possible to estimate a limited number of  $c_{l,n,p}$  coefficients. [Inclusion of additional coefficients, especially in the absence of  $\chi_\lambda(\mathbf{c})$ , results in unreasonably large estimates for the values of the additional coefficients while providing little improvement in the fit of  $\hat{I}^{(\eta, I^{(e)})}(k)$  to  $I^{(e)}(k)$ .] This limitation in the number of coefficients and therefore in the spatial resolution of the reconstructed  $\rho(\mathbf{x})$  is the major cost of a reduced range of  $k$  in the data. Since this cost criterion is insensitive to the signs of  $c_{l,n,p}$ , the signs were set equal to the signs of  $c_{l,n,p}^{(a)}$  in order that the value of  $\epsilon$  correctly reflect the performance of the estimator. Approximately 50 steps of the Levenberg–Marquardt method were required to minimize the cost criterion. Plots of  $\hat{I}^{(12^-, I^{(e)})}(k)$ ,  $\hat{A}_{l,n}^{(12^-, I^{(e)})}(r)$ , and  $\hat{\rho}^{(12^-, I^{(e)})}(\mathbf{x})$  are given in Figs. 5–8.

Because, as shown in Fig. 5, the solution scattering computed from the atomic resolution model ( $I^{(a)}(k)$ ) is only a moderately good fit to the experimental solution scattering data ( $I^{(e)}(k)$ ), there is no gold standard against which the reconstruction  $\hat{A}_{l,n}^{(12^-, I^{(e)})}(r)$  or  $\hat{\rho}^{(12^-, I^{(e)})}(\mathbf{x})$  can be compared. However, as shown in the figures, the reconstruction is consistent with the atomic resolution structure and also with the cryo-electron microscopy reconstruction [20].

## VII. DISCUSSION

In this paper, we have described the first method for computing general 3-D reconstructions of icosahedrally symmetric objects from measurements of the spherical average of the magnitude-squared of the object’s Fourier transform. The method is based on *maximum likelihood* or *maximum a posteriori* estimation of the parameters in a mathematical model of the object. The mathematical model is an orthonormal expansion in spherical coordinates where the angular functions are icosahedral harmonics, which guarantee the icosahedral symmetry of the resulting reconstruction; the radial functions are linear combinations of spherical Bessel functions, which guarantee

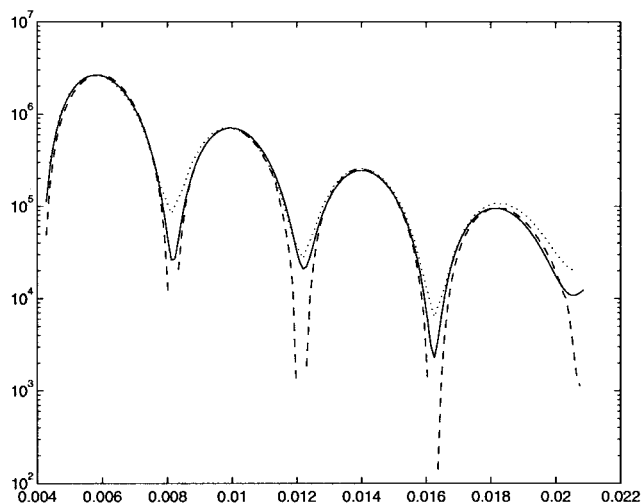


Fig. 5. Solution x-ray scattering data  $I(k)$ :  $I^{(e)}(k)$  (dashed curve),  $\hat{I}^{(12^-, I^{(e)})}(k)$  (solid curve), and  $I^{(a)}(k)$  (dotted curve). Notice that the solution scattering computed from the atomic resolution model ( $I^{(a)}(k)$ ) is only a moderately good fit to the experimental solution scattering data ( $I^{(e)}(k)$ ) and that  $\hat{I}^{(12^-, I^{(e)})}(k)$  attempts to fit  $I^{(e)}(k)$  and not  $I^{(a)}(k)$ .

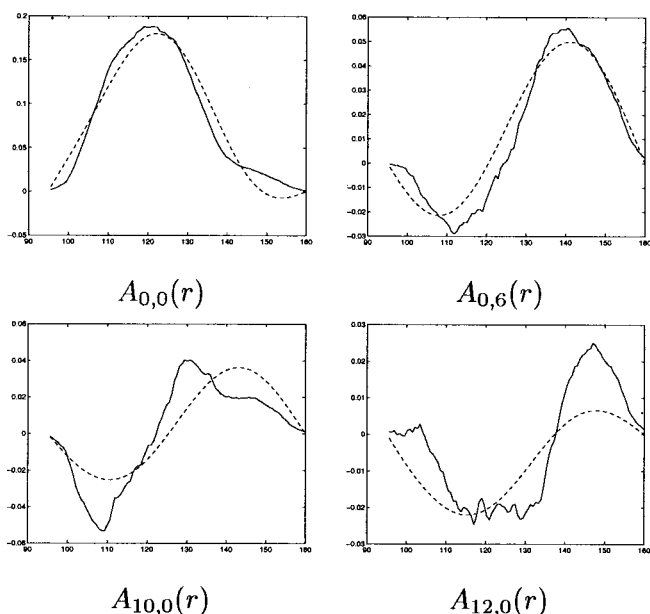


Fig. 6. Icosahedral harmonic expansion coefficients  $A_{l,n}(r)$ :  $A_{l,n}^{LP}(r)$  (solid curve) and  $\hat{A}_{l,n}^{(12^-, I^{(e)})}(r)$  (dashed curve). As shown in Fig. 5, the solution scattering computed from the atomic resolution model ( $I^{(a)}(k)$ ) is only a moderately good fit to the experimental solution scattering data ( $I^{(e)}(k)$ ). Therefore, it is not unexpected that the estimated  $\hat{A}_{l,n}^{(12^-, I^{(e)})}(r)$  functions, which attempt to fit the experimental  $I^{(e)}(k)$  data, disagree to some extent with the computed  $A_{l,n}^{LP}(r)$  functions, which are computed from the atomic resolution model. [ $A_{l,n}^{(a)}(r)$  are impulsive.]

the support constraints on the resulting reconstruction; and the parameters are the weights in the expansion. Measurements of this type are inherently ambiguous. To address this problem, we have proposed a method using two sets of measurements where the second measurement comes from a modified version of the particle. While we have only considered spherical

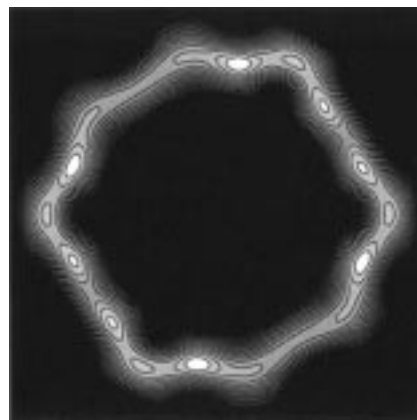


Fig. 7. Contour plot of a cross section in the  $z$ - $x$  plane of the electron density  $\rho(\mathbf{x})$ :  $\hat{\rho}^{(12^-, I^{(e)})}(\mathbf{x})$ . The image is thresholded at zero.



Fig. 8. Stereo images of a contour surface, in 3-D, of the electron density  $\rho(\mathbf{x})$ :  $\hat{\rho}^{(12^-, I^{(e)})}(\mathbf{x})$ . The surface shown is the surface at 10% of the maximum electron density value.

averaging, similar methods can be applied when the data comes from cylindrical averaging.

Measurements of this type occur in solution x-ray scattering problems, and we have described several reconstructions, including a reconstruction from experimental data, where the object in solution is Cowpea mosaic virus. We have considered synthetic data where the model used to compute the synthetic data is in the class of models used to compute the reconstruction and thus perfect reconstructions are possible. Even in the presence of realistic levels of noise, the mean of the ratio of the  $L_2$  norm of the reconstruction error divided by the  $L_2$  norm of the true object is only 0.069. When reconstructions are based on two synthetic data sets, one from the particle and one from the modified version of the particle, and both data sets have realistic levels of noise, then a complete set of correct signs for the unknown parameters can be determined in 73% of the trials. We have also considered synthetic data where the model used to compute the synthetic data is outside the class of models used to compute the reconstruction, and in fact would require an infinite number of parameters to achieve an exact reconstruction. We demonstrated that the number of parameters used in the reconstruction must depend on the amount of data available and we demonstrated the importance of the *a priori* model. Finally, we have considered experimental data and achieved a reconstruction consistent with both the atomic-resolution structure based on x-ray crystallography and the moderate-resolution structure based on cryo-electron microscopy.

These methods can contribute to biophysics by providing a new method for the study of virus structures without crystallization, by providing initial conditions for virus reconstructions based on crystal x-ray diffraction data, and by allowing the study of virus dynamics, such as the changes in structure that occur during the process of infection.

#### ACKNOWLEDGMENT

The authors thank Dr. J. E. Johnson of the Department of Molecular Biology, The Scripps Research Institute, for many helpful discussions and for providing the CpMV data.

#### REFERENCES

- [1] R. P. Millane, "Phase retrieval in crystallography and optics," *J. Opt. Soc. Amer. A*, vol. 7, pp. 394–411, 1990.
- [2] T. Schmidt, J. E. Johnson, and W. E. Phillips, "The spherically averaged structures of Cowpea mosaic virus components by x-ray solution scattering," *Virology*, vol. 127, pp. 65–73, 1983.
- [3] J. T. Finch and K. C. Holmes, "Structural studies of viruses," *Methods in Virology*, vol. III. New York: Academic, 1967.
- [4] Y. Zheng, P. C. Doerschuk, and J. E. Johnson, "Determination of three-dimensional low-resolution viral structure from solution x-ray scattering data," *Biophys. J.*, vol. 69, pp. 619–639, Aug. 1995.
- [5] A. Jack and S. C. Harrison, "On the interpretation of small-angle x-ray solution scattering from spherical viruses," *J. Molec. Biol.*, vol. 99, pp. 15–25, 1975.
- [6] J. D. Jackson, *Classical Electrodynamics*, 2nd ed. New York: Wiley, 1975.
- [7] Y. Zheng and P. C. Doerschuk, "Explicit orthonormal fixed bases for spaces of functions that are totally symmetric under the rotational symmetries of a platonic solid," *Acta Cryst.*, vol. A52, pp. 221–235, 1996.
- [8] ———, "Symbolic symmetry verification for harmonic functions invariant under polyhedral symmetries," *Comput. Phys.*, vol. 9, pp. 433–437, July/Aug. 1995.
- [9] N. V. Cohan, "The spherical harmonics with the symmetry of the icosahedral group," in *Proc. Camb. Phil. Soc.*, vol. 54, pp. 28–38, 1958.
- [10] O. Laporte, "Polyhedral harmonics," *Z. Naturforsch.*, vol. 3a, pp. 447–456, 1948.
- [11] J. Raynal, "Determination of point group harmonics for arbitrary  $j$  by a projection method. II. Icosahedral group, quantization along an axis of order 5," *J. Math. Phys.*, vol. 25, pp. 1187–1194, May 1984.
- [12] ———, "On a labeling for point group harmonics. II. Icosahedral group," *J. Math. Phys.*, vol. 26, pp. 2441–2456, Oct. 1985.
- [13] P. M. Morse and H. Feshbach, *Methods of Theoretical Physics*. New York: McGraw-Hill, 1953.
- [14] E. A. Coddington and N. Levinson, *Theory of Ordinary Differential Equations*. New York: McGraw-Hill, 1955.
- [15] W. R. Wikoff *et al.*, "The structure of a neutralized virus: Canine parvovirus complexed with neutralizing antibody fragment," *Structure*, vol. 2, pp. 595–607, July 15, 1994.
- [16] J. Thygesen, S. Weinstein, F. Franceschi, and A. Yonath, "The suitability of multi-metal clusters for phasing in crystallography of large macromolecular assemblies," *Structure*, vol. 4, pp. 513–518, 1996.
- [17] W. H. Press, B. P. Flannery, S. A. Teukolsky, and W. T. Vetterling, *Numerical Recipes in C: The Art of Scientific Computing*, 2nd ed. Cambridge, U.K.: Cambridge Univ. Press, 1992.
- [18] Z. Chen, C. V. Stauffacher, and J. E. Johnson, "Capsid structure and RNA packaging in comoviruses," *Seminars Virol.*, vol. 1, pp. 453–466, 1990.
- [19] Y. Zheng, "Symmetry constrained signal reconstruction from spherically averaged Fourier transform intensities," Ph.D. dissertation, Purdue Univ., West Lafayette, IN, May 1996.
- [20] J. A. Speir, S. Munshi, G. Wang, T. S. Baker, and J. E. Johnson, "Structures of the native and swollen forms of Cowpea chlorotic mottle virus determined by x-ray crystallography and cryo-electron microscopy," *Structure*, vol. 3, pp. 63–78, Jan. 15, 1995.



**Yibin Zheng** (S'93–M'96) received the B.S.E.E. degree from Zhongshan University, China, in 1988, the M.A. and Ph.D. degrees in physics from the State University of New York at Buffalo in 1992, and the Ph.D. degree in electrical engineering from Purdue University, West Lafayette, IN, in 1996.

He is currently with GE Corporate Research and Development, Schenectady, NY. His research interests include statistical signal processing, numerical and symbolic computing for science and engineering, and mathematical physics.



**Peter C. Doerschuk** (S'79–M'86) received the B.S., M.S., and Ph.D. degrees in electrical engineering from the Massachusetts Institute of Technology (MIT), Cambridge, in 1977, 1979, and 1985, respectively, and the M.D. degree from Harvard Medical School, Cambridge, in 1987.

After post-graduate training at Brigham and Womens' Hospital, he held a post-doctoral appointment at the Laboratory for Information and Decision Systems, MIT, from January 1988 to August 1990. Since August 1990, he has been on the faculty in the School of Electrical and Computer Engineering, Purdue University, West Lafayette, IN.